Distinguishing Different Stackings in Layered Materials via Luminescence Spectroscopy

Matteo Zanfrognini, Alexandre Plaud, Ingrid Stenger, Frédéric Fossard, Lorenzo Sponza, Léonard Schué, Fulvio Paleari, Elisa Molinari, Daniele Varsano, Ludger Wirtz, et al.

Distinguishing Different Stackings in Layered Materials via Luminescence Spectroscopy

Matteo Zanfrognini,[1,2] Alexandre Plaud,[3,4] Ingrid Stenger,[4] Frédéric Fossard,[3] Lorenzo Sponza,[3] Léonard Schué,[3,4] Fulvio Paleari,[2,*] Elisa Molinari,[1,2] Daniele Varsano,[2] Ludger Wirtz,[5] François Ducastelle,[3] Annick Loiseau,[3,†] and Julien Barjon[4,‡]

[1]*Dipartimento di Scienze Fisiche, Informatiche e Matematiche, Università di Modena e Reggio Emilia, I-41125 Modena, Italy*
[2]*Centro S3, CNR-Istituto Nanoscienze, I-41125 Modena, Italy*
[3]*Université Paris-Saclay, ONERA, CNRS, Laboratoire d'étude des microstructures, 92322 Châtillon, France*
[4]*Université Paris-Saclay, UVSQ, CNRS, GEMaC, 78000 Versailles, France*
[5]*Department of Physics and Materials Science, University of Luxembourg, 1511 Luxembourg, Luxembourg*

(Received 29 May 2023; accepted 12 October 2023)

Despite its simple crystal structure, layered boron nitride features a surprisingly complex variety of phonon-assisted luminescence peaks. We present a combined experimental and theoretical study on ultraviolet-light emission in hexagonal and rhombohedral bulk boron nitride crystals. Emission spectra of high-quality samples are measured via cathodoluminescence spectroscopy, displaying characteristic differences between the two polytypes. These differences are explained using a fully first-principles computational technique that takes into account radiative emission from "indirect," finite-momentum excitons via coupling to finite-momentum phonons. We show that the differences in peak positions, number of peaks, and relative intensities can be qualitatively and quantitatively explained, once a full integration over all relevant momenta of excitons and phonons is performed.

DOI:

The microscopic control of Van der Waals stacking configurations is emerging as an important tool for the engineering of the optoelectronic properties of layered materials. In graphite, for example, rhombohedral stacking may result in nontrivial topological properties [1], while the asymmetry of the interlayer coupling resulting from the same stacking motif leads to the emergence of ferroelectricity in transition metal dichalcogenides [2,3], as well as increased effective mobilities due to the change in interlayer coupling strength [4]. The local changes in stacking order in twisted boron nitride (BN) layers again give rise to ferroelectric domains [5]. Understanding the impact of single-layer stacking configurations on the electronic properties of Van der Waals materials is thus of paramount importance. Consequently, exploring BN polytypes serves as an exemplary platform for such investigations. Layered BN crystals are identified as strategic materials for the integration of graphene and 2D semiconductors in optoelectronic devices based on Van der Waals heterostructures [6–8]. To this end, largely scalable crystal growth methods able to produce high-quality samples are desirable. The highest-quality BN single crystals are mostly grown from a catalytic melt either at high pressure and high temperature [9–11] or, more recently, at intermediate or atmospheric pressure and high temperature [12–16]. The resulting crystals are limited in size or polycrystalline, which restricts their possible applications to optoelectronics. Up-scalable fabrication techniques at low pressure, such as chemical vapor deposition or molecular beam epitaxy, allow instead for the controlled synthesis of BN thin films on large surfaces. However, they have encountered a limited success up to now due to the polymorphism of boron nitride. The layered bulk crystal can come, in principle, in six different polytypes [17], with the two most stable ones adopting the hexagonal (hBN) and rhombohedral (rBN) Bravais lattices. In hBN, two adjacent BN single layers differ by a π rotation, resulting in the so-called AA' stacking sequence, where boron and nitrogen atoms sit on top of each other [Fig. 1(a)]. Conversely, the unit cell of rBN crystals is composed of three BN monolayers, which are rigidly shifted along the same direction by the B-N planar interatomic distance: this stacking motif (ABC sequence) is shown in Fig. 1(b). While this stacking

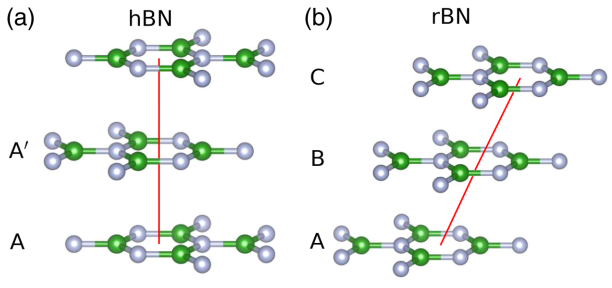

FIG. 1. Stacking sequences of sp_2 BN considered in this work: in (a) boron nitride with AA' stacking is shown, while in (b) the three shifted layers forming rBN unit cell are presented. Nitrogen and boron atoms are shown in gray and green, respectively.

difference entails an extremely high energy cost associated to the transformation from rBN to hBN [18], these two polytypes are difficult to distinguish experimentally from a crystallographic point of view. Even from a computational point of view, the calculated stability difference of the two polytypes is close to the limit of accuracy of modern *ab initio* methods [17,19,20]. In addition, the interaction with the substrate affects the abundance of stable rBN and hBN phases in synthetic products [21–24]. For these reasons, the stacking sequence is rarely characterized in recent reports about BN multilayer growth, so that possible differences in the respective optoelectronic properties of the two polytypes might have been overlooked.

In this Letter, we present a spectroscopic investigation of rBN using cathodoluminescence (CL) spectroscopy. By comparing CL spectra obtained for rBN with analogous results for hBN [25,26], we demonstrate that the stacking sequence affects the emission fine structure of rBN and hBN crystals, making CL an ideal experimental probe to discriminate between the two polytypes. Our experimental observations are explained by *ab initio* calculations of luminescence spectra for the two polytypes, explicitly including exciton-phonon interactions.

The reference sample investigated here is the rBN powder fabricated by T. Sato [21], which is known as the international standard for the crystallographic diffraction database [27]. To our knowledge, this is the highest-quality rBN single crystal available today. Figure 2(a) presents a transmission electron microscopy (TEM) image of the powder. It consists of cylindrical rBN crystallites with a typical 200 nm diameter and a 50 nm thickness. The ABC stacking sequence can be observed in the high-resolution image of the transverse section reported in Fig. 2(b). The distance between B and N in this projection is 0.072 nm, which cannot be resolved due to our 0.12 nm TEM limit resolution. Nevertheless, the positions of B and N atomic columns can be identified in Fig. 2(c) thanks to simulations performed in the conditions of the image acquisition in Fig. 2(d) (see Supplemental Material [28] for details). The identification of the rBN structure is further confirmed by comparing its Raman spectrum with the one of hBN as presented in the Supplemental Material [28] section on Raman spectroscopy. In the following, the properties of the reference rBN sample (ABC stacking) will be compared with a reference hBN crystal grown by high pressure and high temperature [11].

We now turn to the discussion of the exciton-dominated luminescence spectra as studied by CL using the setup detailed in Supplemental Material [28]. A comparison between the experimental CL spectra of hBN and rBN at $T = 5$ K is shown in Fig. 3. The visible features are due to phonon-assisted excitonic recombinations as will be discussed below. The two spectra display several key differences, including a redshift of the rBN features with respect to the corresponding hBN ones (which amounts to 15 meV for the highest peak), and, most importantly, the presence of two relevant structures at 5.847 and 5.919 eV only in rBN. The high accuracy of the experimental rBN spectrum is crucial to clearly resolve the fine structure of the intrinsic phonon-assisted peaks [17,42], enabling us to explain these points in conjunction with the theoretical modeling in the following. Experimentally, these reported differences are fully significant, as we obtained almost identical spectra from a rBN sample grown by chemical vapor deposition on 6H-SiC. A detailed comparison between the two samples is included in Supplemental Material [28], along with a discussion of the defect peaks appearing in the CL signal measured at frequencies lower than those shown in Fig. 3.

Ab initio calculations [43] indicate that rBN is an indirect band-gap insulator. The exciton dispersion resulting from the solution of the Bethe-Salpeter equation at finite momentum is indirect as well, its minimum being located near the point $\Omega = [\frac{1}{6}, \frac{1}{6}, 0]$ in the middle of the ΓK symmetry direction in the hexagonal Brillouin zone (hBZ). According to our calculation, the energy difference between the lowest-lying exciton (due to indirect electronic transition) and the optically accessible (i.e., direct and

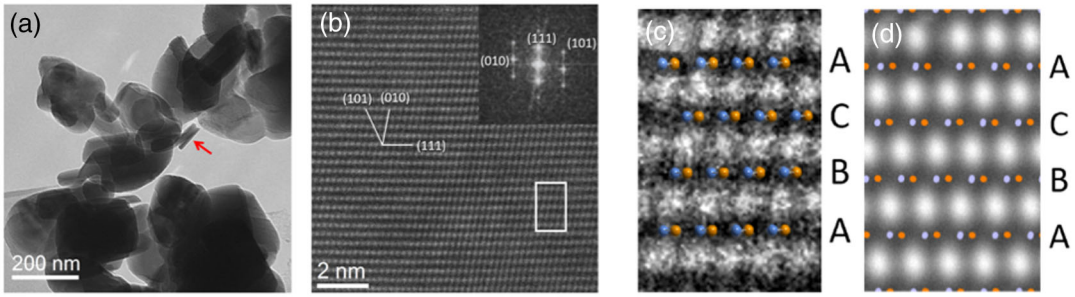

FIG. 2. (a) Bright field TEM image of the reference rBN powder. (b) High resolution TEM image in the $[10\bar{1}]$ zone axis of the crystallite indicated by the red arrow in (a). The traces of (101), (001), and (111) rBN planes reported with white lines are identified with the Fourier transform plotted in inset. (c) Magnified image of the white rectangle in (b) where the atomic positions of B and N (colored spheres) are deduced from the simulation (d), which has been performed with the illumination conditions used experimentally. Crystallographic notations refer here to the rhombohedral phase (see Supplemental Material [28] for details).

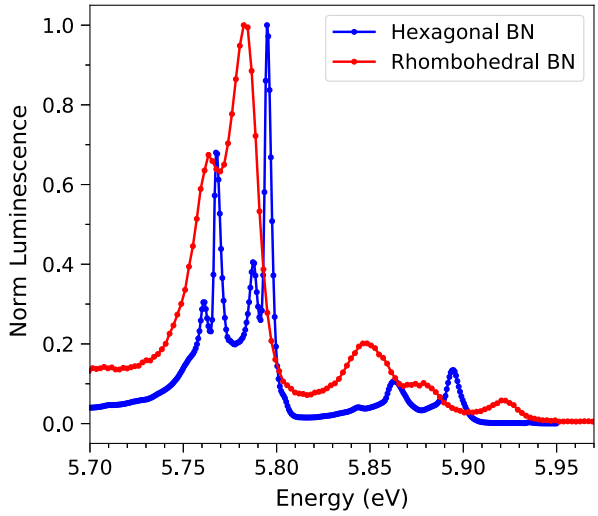

FIG. 3. Comparison of experimental hBN (blue) and rBN (red) CL spectra at $T = 5$ K.

dipole-allowed) Γ excitons is 230 meV (see Supplemental Material [28] for the exciton dispersion curve computed along this direction). This means that the excitonic radiative recombination in rBN requires the assistance of phonons with a wave vector around the Ω point, similarly to what happens in hBN.

The theoretical luminescence spectra have been computed using the expression [44,45]

$$I(E) \propto \sum_{\lambda} \sum_{\mathbf{Q}} \sum_{\nu} N[E_{\lambda}(\mathbf{Q})] \Gamma_{\lambda}^{\nu,\mathbf{Q}}(E), \tag{1}$$

where λ is an index running over exciton bands, $\mathbf{Q}$ is the exciton momentum, and ν denotes the phonon branches. $N[E_{\lambda}(\mathbf{Q})] = e^{-[(E_{\lambda}(\mathbf{Q})-\mu)/k_B T_{\mathrm{exc}}]}$ is a Boltzmann distribution representing the exciton population from which light emission occurs, μ being the energy of the lowest-energy exciton in the system and T_{exc} the effective excitonic temperature. We fixed T_{exc} to 20 K, which is its experimental value obtained for low sample temperatures (below 10 K, as in Fig. 3). (We have checked that our results are stable with respect to small changes of this parameter).

The probability $\Gamma_{\lambda}^{\nu,\mathbf{Q}}(E)$ describes photon emission by a finite-momentum exciton $|\lambda, \mathbf{Q}\rangle$, assisted by a phonon $(\nu, \mathbf{Q})$. This quantity has been computed using second-order time-dependent perturbation theory, similarly to Refs. [46,47], only considering phonon emission processes [48] (which dominate at small temperature):

$$\Gamma_{\lambda}^{\nu,\mathbf{Q}}(E) = |T_{\lambda}^{\nu,\mathbf{Q}}|^2 \frac{(1 + n_{\nu,\mathbf{Q}})\delta[E - E_{\lambda}(\mathbf{Q}) + \hbar\omega_{\nu,\mathbf{Q}}]}{E_{\lambda}(\mathbf{Q}) - \hbar\omega_{\nu,\mathbf{Q}}}, \tag{2}$$

with

$$T_{\lambda}^{\nu,\mathbf{Q}} = \sum_{\lambda_2} \frac{D_{\lambda_2} G_{\lambda_2,\lambda}^{\nu}(\mathbf{Q}, -\mathbf{Q})}{E_{\lambda_2}(\Gamma) + \hbar\omega_{\nu,\mathbf{Q}} - E_{\lambda}(\mathbf{Q})}. \tag{3}$$

In Eqs. (2) and (3), the index λ_2 runs over the excitonic states at the Γ point with energy $E_{\lambda_2}(\Gamma)$. The quantity D_{λ_2} is the excitonic optical dipole strength averaged over in-plane polarization directions. $n_{\nu,\mathbf{Q}}$ corresponds to the Bose-Einstein phonon occupation factor, while E is the energy of the emitted photon; the Dirac delta guarantees energy conservation and has been numerically approximated with a Lorentzian function with FWHM equal to 5 meV in order to match the experimental peaks. Finally, the exciton-phonon coupling matrix element $G_{\lambda_2,\lambda}^{\nu}(\mathbf{Q}, -\mathbf{Q})$ describes the scattering amplitude for an exciton $|\lambda, \mathbf{Q}\rangle$ to states $|\lambda_2, \Gamma\rangle$ while assisted by phonon mode ν [45]:

$$\begin{aligned} &G_{\lambda_2,\lambda}^{\nu}(\mathbf{Q}, -\mathbf{Q}) \\ &= \sum_{vcc'\mathbf{k}} A_{\lambda_2}^{*\Gamma}(v\mathbf{k}, c\mathbf{k}) A_{\lambda}^{\mathbf{Q}}(v\mathbf{k}, c'\mathbf{k} + \mathbf{Q}) g_{cc'}^{\nu}(\mathbf{k} + \mathbf{Q}; -\mathbf{Q}) \\ &\quad - \sum_{vv'c\mathbf{k}} A_{\lambda_2}^{*\Gamma}(v\mathbf{k}, c\mathbf{k}) A_{\lambda}^{\mathbf{Q}}(v'\mathbf{k} - \mathbf{Q}, c\mathbf{k}) g_{v'v}^{\nu}(\mathbf{k}; -\mathbf{Q}), \end{aligned} \tag{4}$$

where $A_{\lambda}^{\mathbf{Q}}(v\mathbf{k}_h, c\mathbf{k}_c)$ is the envelope function for exciton $|\lambda, \mathbf{Q}\rangle$, with v, v' (c, c') running over the valence (conduction) states and $\mathbf{k}$ being the electronic wave vector in the hBZ. The electron-phonon coupling matrix element $g_{n,n'}^{\nu}(\mathbf{k}, \mathbf{Q})$ represents the scattering between single-particle states $|n', \mathbf{k}\rangle$ and $|n, \mathbf{k} + \mathbf{Q}\rangle$ [49]. Importantly, within our numerical methodology, $G_{\lambda_2,\lambda}^{\nu}(\mathbf{Q}, -\mathbf{Q})$ is computed using the same single-particle Kohn-Sham states both for electron-phonon and excitonic quantities, thus overcoming phase mismatch problems as described in Ref. [47]. The $\mathbf{Q}$ integration appearing in Eq. (1) has been performed in local neighborhoods of the symmetry-equivalent Ω points corresponding to the excitonic dispersion minima in the hBZ. The computational details [50] needed to reproduce the theoretical results are provided in the Supplemental Material [28].

In Fig. 4, we present the comparison between experimental CL spectra (black dots) and theoretical Bethe-Salpeter equation results (continuous green lines) for hBN [Fig. 4(a)] and rBN (Fig. 4(c)]. Figures 4(b) and 4(d) show the calculated in-plane phonon dispersion along the ΓK direction for hBN and rBN, respectively. We find very good agreement between experimental and theoretical data. The relative energy shift between the two spectra is reproduced theoretically. As the phonon energies in the two systems differ only for a few meV, the 15 meV shift closely matches the underlying difference between the lowest-lying, finite-momentum exciton levels (which is around 12 meV). In turn, this difference can be traced back to the combined effects of rBN having both a smaller quasiparticle band gap (by 166 meV) and exciton binding energy (by 150 meV)

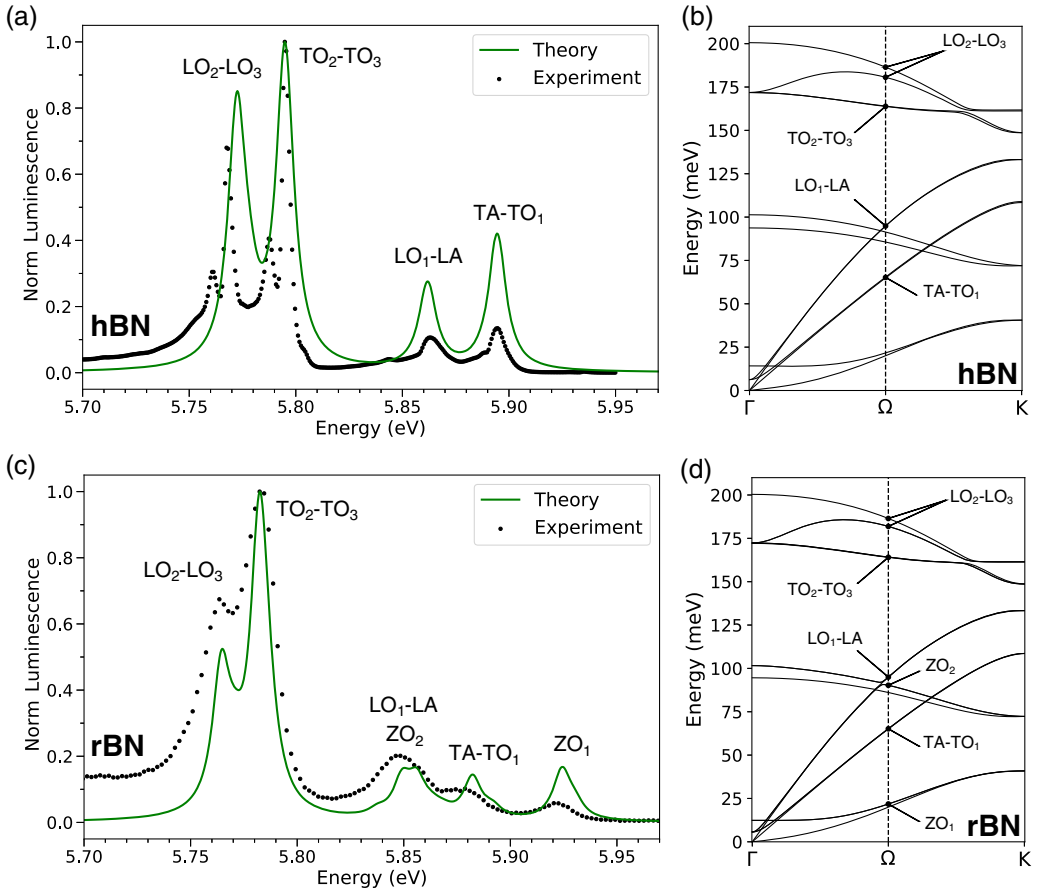

F4:1 FIG. 4. Experimental (black dots) and theoretical (green lines) luminescence spectra for hBN (a) and rBN (c). In both (a) and (c),
F4:2 theoretical spectra are blueshifted by 1.04 eV to match the position of the highest intensity peak in the experimental spectrum (in order to
F4:3 compensate for the systematic theoretical undercorrection of the *GW* quasiparticle band gap in BN). Phonon dispersions in hBN (b) and
F4:4 rBN (d) along the Γ-K direction: phonon branches contributing to the luminescence spectra are highlighted at the Ω point, in the middle
F4:5 of the Γ-K direction. See the main text for the phonon mode labeling. Almost-degenerate phonon branches are paired with a hyphen.

with respect to hBN around the Ω points in momentum space. In both hBN and rBN, the spectra are dominated by the two peaks in the low-energy part of the spectrum. These are phonon-assisted satellites due to longitudinal optical phonons—denoted as LO_2-LO_3 modes in the phonon dispersion—and transverse optical ones (the almost-degenerate pair [56] TO_2-TO_3). For hBN, these assignments are in good agreement with the results obtained in Refs. [46,57], using a finite-difference approach. Furthermore, the experimental intensity ratio between these peaks is well-reproduced by *ab initio* calculations, with the LO peak being less intense than the TO one. The additional overtones appearing in the measurements in this energy region are due to higher-order scattering processes [58] and are thus not captured by our theoretical approach, which is restricted to first-order exciton-phonon interaction. The phonon branches involved in the emission process are explicitly labeled in Figs. 4(b) and 4(d) for the Ω point only [59]. Luminescence spectra of hBN and rBN are qualitatively different at higher energies, as confirmed by *ab initio* results. In the case of hBN, we observe only two main peaks: the first (at about 5.86 eV) corresponds to a replica of the LO_1-LA phonons, while the higher intensity structure at 5.89 eV is mainly due to TO phonons, with a small contribution from the almost-degenerate transverse acoustic mode (TA-TO_1). *Ab initio* results reproduce with great accuracy both the splitting between these peaks and their intensity ratio (the LO_1-LA peak being less pronounced than the TO_1-TA one), while they tend to overestimate their relative strengths, with respect to the dominant, low-energy satellites. [The agreement may be further improved with a more complete **Q**-point integration in Eq. (1).] We also note that, in agreement with the group theory analysis discussed in Ref. [57], no contributions from the out-of-plane phonon modes appear in the luminescence spectra. This selection rule, which is strictly respected by Eq. (4), can be slightly broken in a real experiment, leading to the appearance of a very small signal corresponding to this mode (usually 100 times smaller than the other peaks [60]).

In the case of rBN, the high-energy portion of the CL spectrum shows three large peaks, respectively at about

5.847, 5.878, and 5.919 eV, instead of the two peaks appearing in hBN. They are also recovered in the *ab initio* results. The first structure is a combination of phonon-assisted replicas due to the almost-degenerate LA-LO_1 branches, albeit with a relevant contribution from optical out-of-plane modes (denoted as ZO_2; see Supplemental Material [28] for a mode-resolved spectrum). Conversely, the peak at 5.878 eV is associated to the TA-TO_1 phonons in analogy with the hBN case. We emphasize that *ab initio* results correctly reproduce the intensity ratio among these peaks. Finally, the highest-energy structure at 5.919 eV turns out to be due to the out-of-plane optical mode ZO_1. This is forbidden for the centrosymmetric hBN luminescence while it is allowed in the rBN case because of the lowered symmetry of the crystal lattice.

In conclusion, we have demonstrated that cathodoluminescence is a viable tool to characterize fundamentally similar BN polytypes, which are hardly distinguishable otherwise. We have explained both experimentally and theoretically how the radiative emission spectrum is affected by the interaction between electronic excitations and lattice vibrations in rhombohedral and hexagonal boron nitride, two prototypical polytypes of low-dimensional layered materials with indirect band gap. Using a first-principles methodology that accounts for exciton-phonon interactions beyond the state of the art, we are able to provide a comprehensive and accurate description of the finite-momentum exciton states and phonon modes involved, thus showing the discriminating role of out-of-plane lattice vibrations assisting excitonic radiative recombination for rBN but not for hBN. We believe that our analysis and methodology could be useful for the growth and characterization of indirect-gap layered materials, which find widespread application as basic building blocks in novel 2D optoelectronic devices.

The authors would like to thank C. Vilar for the technical support on electron microscopy and K. Watanabe and T. Taniguchi for kindly providing a part of the rBN reference powder of T. Sato, M. Chubarov, and A. Henry for providing rBN whiskers on 6H-SiC. We thank C. Attaccalite and P. Lechifflart for useful discussions about exciton-phonon coupling calculations. This project has received funding from the European Union Horizon 2020 research and innovation programme under Grant Agreements No. 785219 and No. 881603 (Graphene Flagship core 2 and core 3), the French National Agency for Research (ANR) under Grant Agreement No. ANR-14-CE08-0018 (GoBN: Graphene on Boron Nitride Technology), MaX—MAterials design at the eXascale—a European Centre of Excellence funded by the European Union's program HORIZON-EUROHPC-JU-2021-COE-01 (Grant No. 101093374). D. V. and M. Z. also acknowledge financial support from ICSC—Centro Nazionale di Ricerca in High Performance Computing, Big Data and Quantum Computing, funded by European Union—NextGenerationEU—PNRR and the Italian national program PRIN2017 Grant No. 2017BZPKSZ. L. W. acknowledges funding by Fond National de Recherche (FNR), Luxembourg via project INTER/19/ANR/13376969/ACCEPT. We acknowledge EuroHPC Joint Undertaking for awarding us access to MeluXina at LuxProvide, Luxembourg and CINECA for computational resources, awarded via the ISCRA grants.

A. P. and M. Z. contributed equally to this work.

*Corresponding author: fulvio.paleari@nano.cnr.it
†Corresponding author: annick.loiseau@onera.fr
‡Corresponding author: julien.barjon@uvsq.fr

[1] S. Slizovskiy, E. McCann, M. Koshino, and V. I. Fal'ko, Commun. Phys. **2**, 164 (2019).
[2] X. Wang, K. Yasuda, Y. Zhang, S. Liu, K. Watanabe, T. Taniguchi, J. Hone, L. Fu, and P. Jarillo-Herrero, Nat. Nanotechnol. **17**, 367 (2022).
[3] J. Liang, D. Yang, J. Wu, J. I. Dadap, K. Watanabe, T. Taniguchi, and Z. Ye, Phys. Rev. X **12**, 041005 (2022).
[4] X. Li, X. Shi, D. Marian, D. Soriano, T. Cusati, G. Iannaccone, G. Fiori, Q. Guo, W. Zhao, and Y. Wu, Sci. Adv. **9**, eade5706 (2023).
[5] C. R. Woods, P. Ares, H. Nevison-Andrews, M. J. Holwill, R. Fabregas, F. Guinea, A. K. Geim, K. S. Novoselov, N. R. Walet, and L. Fumagalli, Nat. Commun. **12**, 347 (2021).
[6] K. S. Novoselov, A. Mishchenko, A. Carvalho, and A. H. C. Neto, Science **353**, aac9439 (2016).
[7] A. Geim and I. Grigorieva, Nature (London) **499**, 419 (2013).
[8] G. Wang, C. Robert, M. M. Glazov, F. Cadiz, E. Courtade, T. Amand, D. Lagarde, T. Taniguchi, K. Watanabe, B. Urbaszek, and X. Marie, Phys. Rev. Lett. **119**, 047401 (2017).
[9] V. L. Y. Solozhenko, I. A. Petrusha, and A. A. Svirid, High Press. Res. **15**, 95 (1996).
[10] K. Watanabe, T. Taniguchi, and H. Kanda, Nat. Mater. **3**, 404 (2004).
[11] T. Taniguchi and K. Watanabe, J. Cryst. Growth **303**, 525 (2007).
[12] Y. Kubota, K. Watanabe, O. Tsuda, and T. Taniguchi, Science **317**, 932 (2007).
[13] S. Liu, R. He, L. Xue, J. Li, B. Liu, and J. H. Edgar, Chem. Mater. **30**, 6222 (2018).
[14] M. Onodera, T. Taniguchi, K. Watanabe, M. Isayama, S. Masubuchi, R. Moriya, and T. Machida, Nano Lett. **20**, 735 (2020).
[15] J. Sonntag, J. Li, A. Plaud, A. Loiseau, J. Barjon, J. H. Edgar, and C. Stampfer, 2D Mater. **7**, 031009 (2020).
[16] C. Maestre, Y. Li, V. Garnier, P. Steyer, S. Roux, A. Plaud, A. Loiseau, J. Barjon, L. Ren, C. Robert, B. Han, X. Marie, C. Journet, and B. Toury, 2D Mater. **9**, 035008 (2022).
[17] B. Gil, W. Desrat, A. Rousseau, C. Elias, P. Valvin, M. Moret, J. Li, E. Janzen, J. H. Edgar, and G. Cassabois, Crystals **12**, 782 (2022).
[18] W. J. Yu, W. M. Lau, S. P. Chan, Z. F. Liu, and Q. Q. Zheng, Phys. Rev. B **67**, 014108 (2003).

[19] K. Luo, X. Yuan, Z. Zhao, D. Yu, B. Xu, Z. Liu, Y. Tian, G. Gao, and J. He, J. Appl. Phys. **121**, 165102 (2017).

[20] H. Pedersen, B. Alling, H. Högberg, and A. Ektarawong, J. Vac. Sci. Technol. A **37**, 040603 (2019).

[21] T. Sato, Proc. Jpn. Acad. Ser. B **61**, 459 (1985).

[22] P. Sutter, J. Lahiri, P. Zahl, B. Wang, and E. Sutter, Nano Lett. **13**, 276 (2013).

[23] A. Henry, M. Chubarov, Z. Czigány, M. Garbrecht, and H. Högberg, Jpn. J. Appl. Phys. **55**, 05FD06 (2016).

[24] L. Souqui, J. Palisaitis, N. Ghafoor, H. Pedersen, and H. Högberg, J. Vac. Sci. Technol. A **39**, 013405 (2021).

[25] G. Cassabois, P. Valvin, and B. Gil, Nat. Photonics **10**, 262 (2016).

[26] L. Schué, L. Sponza, A. Plaud, H. Bensalah, K. Watanabe, T. Taniguchi, F. Ducastelle, A. Loiseau, and J. Barjon, Phys. Rev. Lett. **122**, 067401 (2019).

[27] Sample (f) in Ref. [21] is known under No 00-045-1171 for the Joint Committee on Powder Diffraction Standards (JCPDS) http://www.icdd.com.

[28] See Supplemental Material at http://link.aps.org/supplemental/10.1103/PhysRevLett.000.000000 for comparisons between the CL spectrum of a different rBN sample, Raman spectra of hBN and rBN, TEM details, defect discussion, and computational details on the *ab initio* density functional theory, density functional perturbation theory, and exciton-phonon calculations including additional data, which includes Refs. [29–41].

[29] L. Schue, Ph.D. thesis, Université Paris-Saclay, 2017.

[30] M. Chubarov, H. Pedersen, H. Högberg, A. Henry, and Z. Czigány, J. Vac. Sci. Technol. A **33**, 061520 (2015).

[31] J. Liu, Y. K. Vohra, J. T. Tarvin, and S. S. Vagarali, Phys. Rev. B **51**, 8591 (1995).

[32] M. van Setten, M. Giantomassi, E. Bousquet, M. Verstraete, D. Hamann, X. Gonze, and G.-M. Rignanese, Comput. Phys. Commun. **226**, 39 (2018).

[33] S. Baroni, S. de Gironcoli, A. Dal Corso, and P. Giannozzi, Rev. Mod. Phys. **73**, 515 (2001).

[34] G. Onida, L. Reining, and A. Rubio, Rev. Mod. Phys. **74**, 601 (2002).

[35] K. Watanabe, T. Taniguchi, T. Kuroda, and H. Kanda, Appl. Phys. Lett. **89**, 141902 (2006).

[36] P. Jaffrennou, J. Barjon, J.-S. Lauret, B. Attal-Trétout, F. Ducastelle, and A. Loiseau, J. Appl. Phys. **102**, 116102 (2007).

[37] A. Pierret, H. Nong, F. Fossard, B. Attal-Tretout, Y. Xue, D. Golberg, J. Barjon, and A. Loiseau, J. Appl. Phys. **118**, 234307 (2015).

[38] L. Bourgeois, Y. Bando, and T. Sato, J. Phys. D **33**, 1902 (2000).

[39] H. Prevost, A. Andrieux-Ledier, N. Dorval, F. Fossard, J. S. Mérot, L. Schué, A. Plaud, E. Héripré, J. Barjon, and A. Loiseau, 2D Mater. **7**, 045018 (2020).

[40] F. Libbi, Pedro Miguel M. C. de Melo, Z. Zanolli, M. J. Verstraete, and N. Marzari, Phys. Rev. Lett. **128**, 167401 (2022).

[41] P. Stadelmann, Ultramicroscopy **21**, 131 (1987).

[42] M. Moret, A. Rousseau, P. Valvin, S. Sharma, L. Souqui, H. Pedersen, H. Högberg, G. Cassabois, J. Li, J. H. Edgar, and B. Gil, Appl. Phys. Lett. **119**, 262102 (2021).

[43] L. Sponza, H. Amara, C. Attaccalite, S. Latil, T. Galvani, F. Paleari, L. Wirtz, and F. Ducastelle, Phys. Rev. B **98**, 125206 (2018).

[44] F. Paleari, Ph. D. thesis, University of Luxembourg, 2019.

[45] H.-Y. Chen, D. Sangalli, and M. Bernardi, Phys. Rev. Lett. **125**, 107401 (2020).

[46] E. Cannuccia, B. Monserrat, and C. Attaccalite, Phys. Rev. B **99**, 081109(R) (2019).

[47] P. Lechifflart, F. Paleari, D. Sangalli, and C. Attaccalite, Phys. Rev. Mater. **7**, 024006 (2023).

[48] G. P. G. Grosso, *Solid State Physics* (Academic Press, New York, 2000).

[49] F. Giustino, Rev. Mod. Phys. **89**, 015003 (2017).

[50] The theoretical spectra have been obtained using Quantum Espresso [51,52] and PERTURBO [53] packages to evaluate ground state electronic properties, vibrational excitations, and electron-phonon matrix elements while exciton energies and wave functions have been obtained using YAMBO [54,55] code. **Q1**

[51] P. Giannozzi *et al.*, J. Phys. Condens. Matter **21**, 395502 (2009). **Q2**

[52] P. Giannozzi *et al.*, J. Phys. Condens. Matter **29**, 465901 (2017).

[53] J.-J. Zhou, J. Park, I.-T. Lu, I. Maliyov, X. Tong, and M. Bernardi, Comput. Phys. Commun. **264**, 107970 (2021).

[54] A. Marini, C. Hogan, M. Grüning, and D. Varsano, Comput. Phys. Commun. **180**, 1392 (2009).

[55] D. Sangalli *et al.*, J. Phys. Condens. Matter **31**, 325902 (2019).

[56] A. Molina-Sánchez and L. Wirtz, Phys. Rev. B **84**, 155413 (2011).

[57] F. Paleari, H. P. C. Miranda, A. Molina-Sánchez, and L. Wirtz, Phys. Rev. Lett. **122**, 187401 (2019).

[58] T. Q. P. Vuong, G. Cassabois, P. Valvin, V. Jacques, R. Cuscó, L. Artús, and B. Gil, Phys. Rev. B **95**, 045207 (2017).

[59] In our labeling of the phonon modes, we chose to disentangle explicitly the almost-degenerate Davydov pairs of modes. This is the reason why, for example, we consider the lowest-energy phonon mode to be a pair of acoustic (ZA) and optical (ZO_1) out-of-plane modes, with only the latter being responsible for the signal in Fig. 4(c). In the experimental literature, this pair is usually labeled jointly as "ZA," and the same goes for the other pairs.

[60] T. Q. P. Vuong, G. Cassabois, P. Valvin, V. Jacques, A. V. D. Lee, A. Zobelli, K. Watanabe, T. Taniguchi, and B. Gil, 2D Mater. **4**, 011004 (2016).